

# Photonic integrated Mach-Zehnder interferometer with an on-chip reference arm for optical coherence tomography

Günay Yurtsever,<sup>1,2,\*</sup> Boris Považay,<sup>3,4</sup> Aneesh Alex,<sup>4</sup> Behrooz Zabihian,<sup>4</sup>  
Wolfgang Drexler,<sup>4</sup> and Roel Baets<sup>1,2</sup>

<sup>1</sup> Photonics Research Group, Ghent University-imec, Sint-Pietersnieuwstraat 41, B-9000 Ghent, Belgium

<sup>2</sup> Center for Nano- and Biophotonics (NB-Photonics), Ghent University, Ghent, Belgium

<sup>3</sup> optoLab, Institute for Human Centered Engineering, Bern University of Applied Sciences, Quellgasse 21, CH-2502 Biel/Bienne, Switzerland

<sup>4</sup> Center for Medical Physics and Biomedical Engineering, Medical University Vienna, General Hospital Vienna 4, L Waehringer Guertel 18-20, A-1090 Vienna, Austria

\*gunay@intec.ugent.be

**Abstract:** Optical coherence tomography (OCT) is a noninvasive, three-dimensional imaging modality with several medical and industrial applications. Integrated photonics has the potential to enable mass production of OCT devices to significantly reduce size and cost, which can increase its use in established fields as well as enable new applications. Using silicon nitride (Si<sub>3</sub>N<sub>4</sub>) and silicon dioxide (SiO<sub>2</sub>) waveguides, we fabricated an integrated interferometer for spectrometer-based OCT. The integrated photonic circuit consists of four splitters and a 190 mm long reference arm with a foot-print of only 10 × 33 mm<sup>2</sup>. It is used as the core of a spectral domain OCT system consisting of a superluminescent diode centered at 1320 nm with 100 nm bandwidth, a spectrometer with 1024 channels, and an x-y scanner. The sensitivity of the system was measured at 0.25 mm depth to be 65 dB with 0.1 mW on the sample. Using the system, we imaged human skin *in vivo*. With further optimization in design and fabrication technology, Si<sub>3</sub>N<sub>4</sub>/SiO<sub>2</sub> waveguides have a potential to serve as a platform for passive photonic integrated circuits for OCT.

©2014 Optical Society of America

**OCIS codes:** (110.4500) Optical coherence tomography; (170.4500) Optical coherence tomography; (130.0130) Integrated optics.

## References and links

1. D. Huang, E. A. Swanson, C. P. Lin, J. S. Schuman, W. G. Stinson, W. Chang, M. R. Hee, T. Flotte, K. Gregory, C. A. Puliafito, and J. G. Fujimoto, "Optical coherence tomography," *Science* **254**(5035), 1178–1181 (1991).
2. M. Wojtkowski, "High-speed optical coherence tomography: basics and applications," *Appl. Opt.* **49**(16), D30–D61 (2010).
3. D. Stifter, "Beyond biomedicine: a review of alternative applications and developments for optical coherence tomography," *Appl. Phys. B* **88**(3), 337–357 (2007).
4. G. Grasso, P. Galli, M. Romagnoli, E. Iannone, and A. Bogoni, "Role of Integrated Photonics Technologies in the Realization of Terabit Nodes [Invited]," *Opt. Commun. Netw.* **1**(3), B111–B119 (2009).
5. I. P. Kaminow, "Optical Integrated Circuits: A Personal Perspective," *J. Lightwave Technol.* **26**(9), 994–1004 (2008).
6. L. Grenouillet, T. Dupont, P. Philippe, J. Harduin, N. Olivier, D. Bordel, E. Augendre, K. Gilbert, P. Grosse, A. Chelnokov, and J. M. Fedeli, "Hybrid integration for silicon photonics applications," *Opt. Quantum Electron.* **44**(12-13), 527–534 (2012).
7. C. R. Doerr and K. Okamoto, "Advances in Silica Planar Lightwave Circuits," *J. Lightwave Technol.* **24**(12), 4763–4789 (2006).
8. G. D. Cole, E. Behymer, T. C. Bond, and L. L. Goddard, "Short-wavelength MEMS-tunable VCSELs," *Opt. Express* **16**(20), 16093–16103 (2008).
9. V. Jayaraman, G. D. Cole, M. Robertson, C. Burgner, D. John, A. Uddin, and A. Cable, "Rapidly swept, ultra-widely-tunable 1060 nm MEMS-VCSELs," *Electron. Lett.* **48**(21), 1331–1333 (2012).

10. M. P. Minneman, J. Ensher, M. Crawford, and D. Derickson, "All-semiconductor high-speed akinetic swept-source for OCT," *Proc. SPIE* **8311**, 831116 (2011).
11. B. W. Tilma, Y. Jiao, J. Kotani, B. Smalbrugge, H. P. M. M. Ambrosius, P. J. Thijs, X. J. M. Leijten, R. Ntzel, M. K. Smit, and E. A. J. M. Bente, "Integrated tunable quantum-dot laser for optical coherence tomography in the 1.7 $\mu$ m wavelength region," *IEEE J. Quantum Electron.* **48**(2), 87–98 (2012).
12. A. Mekis, S. Gloeckner, G. Masini, A. Narasimha, T. Pinguet, S. Sahni, and P. D. Dobbelaere, "A gratingcoupler-enabled CMOS photonics platform," *IEEE J. Sel. Top. Quantum Electron.* **17**(3), 597–608 (2011).
13. L. Zhuang, D. Marpaung, M. Burla, W. Beeker, A. Leinse, and C. Roeloffzen, "Low-loss, high-index-contrast Si<sub>3</sub>N<sub>4</sub>/SiO<sub>2</sub> optical waveguides for optical delay lines in microwave photonics signal processing," *Opt. Express* **19**(23), 23162–23170 (2011).
14. D. Culemann, A. Knuettel, and E. Voges, "Integrated optical sensor in glass for optical coherence tomography," *IEEE J. Sel. Top. Quantum Electron.* **6**(5), 730–734 (2000).
15. G. Yurtsever, K. Komorowska, and R. Baets, "Low Dispersion Integrated Michelson Interferometer on Silicon on Insulator for Optical Coherence Tomography," *Proc. SPIE* **8091**, 80910 (2011).
16. V. D. Nguyen, N. Weiss, W. Beeker, M. Hoekman, A. Leinse, R. G. Heideman, T. G. van Leeuwen, and J. Kalkman, "Integrated-optics-based swept-source optical coherence tomography," *Opt. Lett.* **37**(23), 4820–4822 (2012).
17. B. I. Akca, B. Považay, A. Alex, K. Wörhoff, R. M. de Ridder, W. Drexler, and M. Pollnau, "Miniature spectrometer and beam splitter for an optical coherence tomography on a silicon chip," *Opt. Express* **21**(14), 16648–16656 (2013).
18. F. Morichetti, A. Melloni, M. Martinelli, R. G. Heideman, A. Leinse, D. H. Geuzebroek, and A. Borreman, "Box-Shaped Dielectric Waveguides: A New Concept in Integrated Optics?" *J. Lightwave Technol.* **25**(9), 2579–2589 (2007).
19. W. Bogaerts and S. K. Selvaraja, "Compact Single-Mode Silicon Hybrid Rib/Strip Waveguide With Adiabatic Bends," *IEEE Photon. J.* **3**(3), 422–432 (2011).
20. M. Izutsu, Y. Nakai, and T. Sueta, "Operation mechanism of the single-mode optical-waveguide Y junction," *Opt. Lett.* **7**(3), 136–138 (1982).
21. B. Hofer, B. Považay, B. Hermann, A. Unterhuber, G. Matz, and W. Drexler, "Dispersion encoded full range frequency domain optical coherence tomography," *Opt. Express* **17**(1), 7–24 (2009).
22. T. Mizuno, Y. Hashizume, M. Yanagisawa, T. Kitoh, A. Kaneko, and H. Takahashi, "Wideband planar lightwave circuit type variable optical attenuator using phase-generating coupler," *Electron. Lett.* **11**(42), 636638 (2006).
23. M. L. V. Tse, H. Y. Tam, L. B. Fu, B. K. Thomas, L. Dong, C. Lu, and P. K. A. Wai, "Fusion splicing holey fibers and Single-Mode Fibers: A simple method to reduce loss and increase strength," *IEEE Photon. Technol. Lett.* **21**(3), 164–166 (2009).
24. I. Moerman, P. P. Van Daele, and P. M. Demeester, "A review on fabrication technologies for the monolithic integration of tapers with III-V semiconductor devices," *IEEE J. Sel. Top. Quantum Electron.* **3**(6), 13081320 (1997).
25. A. M. Rollins and J. A. Izatt, "Optimal interferometer designs for optical coherence tomography," *Opt. Lett.* **24**(21), 1484–1486 (1999).
26. K. Kato and Y. Tohmori, "PLC hybrid integration technology and its application to photonic components," *IEEE J. Sel. Top. Quantum Electron.* **6**(1), 4–13 (2000).

---

## 1. Introduction

Optical coherence tomography (OCT) is an interferometric imaging modality capable of producing cross-sectional, high-resolution images of semi-transparent samples such as biological tissue [1]. OCT can image tissue cross sections with < 10  $\mu$ m axial resolution at depths exceeding 2 cm in transparent tissues (*e.g.* human eye, animal embryos) and 1-2 mm in highly scattering tissues (*e.g.* skin, retina, blood vessel wall). The main applications of OCT are medical, such as in ophthalmology, cardiology and dermatology. Applications in other medical fields, such as gastroenterology, pulmonology, and dentistry may emerge from research to clinic [2]. Industrial applications for material characterization are also being investigated [3]. While OCT is already considered to be an affordable high resolution modality, costs and complexity are still prohibitive for wide spread application in existing and novel areas. Current implementations of OCT systems are commonly based on fiber and discrete free space optical components. Integration of such components on a wafer-level has shown advantages in cost, size, stability and power efficiency for optical network technology [4]. Imaging applications like OCT might benefit from such photonic integration as well.

Photonic integrated circuits (PICs) are analogous to electronic integrated circuits (EICs) in a way that they implement multiple functions on a single monolithic substrate. The fabrication methods of PICs are similar to EICs, where multi layered structures are built on top of carrier substrates, patterned by lithography and further etched, deposited, or altered by diffusion or doping. The basic element of integrated photonics is the waveguide. Other components are usually built by introducing modifications to the simple waveguide structure such as changing the geometry and altering or actively manipulating the physical properties of the waveguide. Devices such as splitters, filters, modulators, amplifiers, lasers, and detectors have been demonstrated in different materials systems [5]. Although it may not be possible to realize all of them optimally on the same material system, different components can be combined on a substrate that is suitable to implement passive structures [6]. Depending on the device, specific material systems are favored. For example, silica PICs are preferred for low-loss, thermally stable passive devices [7]; compound semiconductor (*e.g.* GaAs, InP) PICs are efficient for light sources [8–11]; silicon PICs have the merit of being manufacturable in a CMOS fab [12]; and silicon nitride ( $\text{Si}_3\text{N}_4$ ) PICs are transparent in the visible and infrared regions and permit moderately small waveguide bend radii [13].

One of the OCT components that can be integrated on a chip is the interferometer. Some research groups have already demonstrated integrated interferometers for OCT using different material systems. Culeman et al. reported on parallel integration of eight Michelson interferometers implemented in glass [14]. Their design was used as part of a time domain OCT to image human skin. Yurtsever et al. demonstrated a Michelson interferometer implemented in silicon on insulator [15]. The sensitivity of that system was not sufficient for *in vivo* imaging. Recently, Nguyen et al. fabricated a Michelson interferometer using  $\text{Si}_3\text{N}_4$  and silicon dioxide ( $\text{SiO}_2$ ) and was used in a swept-source OCT system to obtain an image of an *in vitro* tissue phantom [16]. In another recent study, Akca et al. demonstrated a beam splitter and an arrayed waveguide grating on chip for OCT in silicon oxynitride ( $\text{SiON}$ ) [17]. Although the waveguides in those studies are sufficiently low loss to implement a long reference arm, none of these four designs had a sufficiently long on-chip reference arm to compensate the optical path length of an x-y scanner. Therefore, they used an external reference arm or required scanning of the sample or the chip to obtain an image. Short on-chip reference arms in those studies could have been chosen to further miniaturize the device or to demonstrate a simple proof of concept device.

In this work, we present the design, characterization and application of a Mach-Zehnder interferometer-based PIC consisting y-splitters and an on-chip 190 mm long (physical length) reference arm. The chip completely replaces the interferometer in a spectrometer-based OCT system. The splitters and the reference arm are realized with broadband, low loss (0.14 dB/cm)  $\text{Si}_3\text{N}_4/\text{SiO}_2$  waveguides. In this system, broadband light from a superluminescent LED (SLED) centered at 1320 nm with 100 nm bandwidth is coupled to the integrated interferometer, part of the light is directed to the on-chip reference arm, and part of the light is sent out of the chip via the sample arm to a galvanometric x-y scanner. The light returning from the reference and the sample arms are combined on the chip's combiner and sent to an external spectrometer. In the following sections, we describe the detailed design and characterization of the on-chip interferometer and present *in vivo* OCT images of human skin.

## 2. Design of the photonic integrated circuit and the OCT setup

### 2.1 Waveguide design

The waveguides used in our study are based on  $\text{Si}_3\text{N}_4$  and  $\text{SiO}_2$  waveguide technology called TriPleX™, which was developed by LioniX BV (Enschede, The Netherlands) [18]. Unlike typical two layer waveguides with high index core surrounded by low index cladding, these waveguides are box shaped consisting of three layers. A low index core ( $\text{SiO}_2$ ) is encapsulated in a box shaped high index ( $\text{Si}_3\text{N}_4$ ) layer, which is buried in low index material ( $\text{SiO}_2$ ) as

illustrated Fig. 1(a). The refractive index contrast between  $\text{Si}_3\text{N}_4$  ( $n = 1.98$ ) and  $\text{SiO}_2$  ( $n = 1.45$ ) enables realization of smaller bends compared to doped silica waveguides, which results in smaller circuits. The waveguides are fabricated on a silicon carrier wafer; fabrication process details are described in [18]. A scanning electron microscope cross-section image of a fabricated waveguide is shown in Fig. 1(b). The  $\text{Si}_3\text{N}_4$  layer is visible in dark grey and  $\text{SiO}_2$  appears in light grey color, the thickness of the  $\text{Si}_3\text{N}_4$  layer is 50 nm. The dry etching process used in waveguide definition results in  $82^\circ$  sloped sidewalls rather than perpendicular sidewalls.

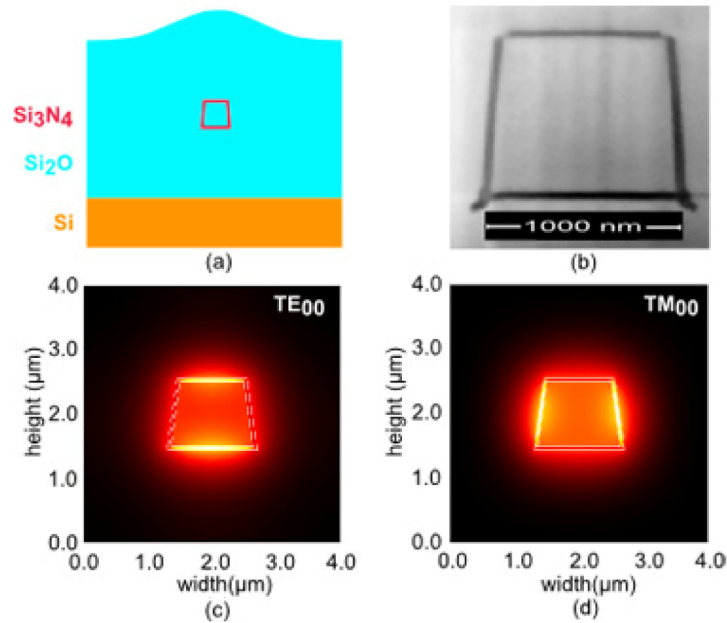


Fig. 1. Box shaped waveguide cross-sections and fundamental mode profiles. (a) Illustration of box shaped  $\text{Si}_3\text{N}_4$  waveguide embedded in  $\text{SiO}_2$  on the Si-carrier. (b) Scanning electron microscope image of waveguide cross-section. (c) Simulated  $\text{TE}_{00}$  intensity mode profile at 1250 nm for a waveguide 1  $\mu\text{m}$  wide and 1  $\mu\text{m}$  high. (d) Simulated  $\text{TM}_{00}$  intensity mode profile at 1250 nm for a waveguide 1  $\mu\text{m}$  wide and 1  $\mu\text{m}$  high.

Interferometers for OCT require single mode waveguides as multimode interferences would degrade axial resolution, sensitivity and stability. To find the condition for single mode operation, we simulated the effective index of the fundamental TE and TM modes for different waveguide widths. Although lithography allows for extremely low costs in mass production, the individual steps are very costly. The design was fabricated in a multi project wafer run, where mask space and process costs are shared with other participants but compromises in the manufacturing technology have to be made. In this particular run, the height of the waveguides was fixed to 1  $\mu\text{m}$  and the  $\text{Si}_3\text{N}_4$  layer thickness was set to 50 nm. Due to the process constraints, only the width of the waveguide could be varied. During the simulations, these fabrication constraints, including the sloped sidewalls were considered. The effective index simulations were performed at 1250 nm, which is the lower spectral end of the superluminescent diode utilized in the OCT system. For the simulations we used the commercially available, fully vectorial mode solver software Fimmwave (Photon Design, Oxford, UK). The calculated TE and TM mode effective indices as a function of waveguide width are given in Fig. 2.

As seen in Fig. 2, when the waveguide width is kept below 1.58  $\mu\text{m}$ , only the fundamental TE and TM modes can propagate. For our design, we chose 1  $\mu\text{m}$  as waveguide width, which is far from the cut-off wavelength and sufficiently wide for lithographic definition. We also

simulated the mode profiles for the fundamental TE and TM modes, as given in Fig. 1(c) and 1(d). Both mode profiles are nearly circular, however, the fundamental TE is more strongly confined in the parallel high index layer, and the fundamental TM mode is more strongly confined in the vertical high index layer. Due to the sloped sidewalls, the TE and TM modes are not completely symmetric which results in different group indices and dispersion. From the simulations, we found the group indices and group velocity dispersions (GVDs) of TE<sub>00</sub> and TM<sub>00</sub> modes at 1320 nm to be (1.489, -347 ps/nm/km) and (1.510, -205 ps/nm/km) respectively. The propagation losses of TE<sub>00</sub> and TM<sub>00</sub> modes are 0.06 dB/cm and 0.14 dB/cm, respectively. Since the propagation losses do not differ significantly among the two modes, we chose the TM<sub>00</sub> mode as it would cause lower dispersion.

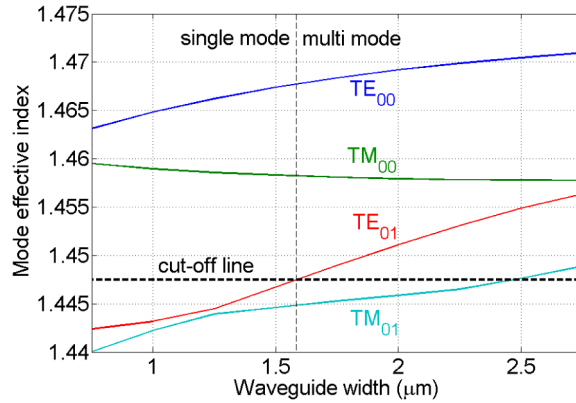


Fig. 2. Calculated effective indices of the TE and TM modes of a box waveguide versus waveguide width at 1250 nm. Waveguide height: 1 μm, Si<sub>3</sub>N<sub>4</sub> layer thickness: 50 nm.

The minimum bend radii of waveguides determine the size of a photonic integrated circuit. The higher the refractive index difference between the core and the cladding, the higher the confinement of the mode, which enables smaller bend radii. Box-shaped TriPleX™ waveguides have moderate size bend radii, which are larger than silicon waveguide bend radii but smaller than silica waveguide bend radii. The transition between a straight waveguide and a circular bend gives rise to a mode mismatch, as the peak of the bend mode is slightly shifted towards the outside of the bend. This mode mismatch causes a small amount of loss and back reflection. It is possible to design bends which adiabatically transform the straight waveguide into a circular one, however, they consume significantly more space than circular bends [19]. Using adiabatic bends it would not be possible to fit the design in the available mask space in this project, thus we used circular bends with minimum bend radius of 2.5 mm.

In this multi wafer project run, symmetric y-splitter and directional coupler designs were provided as building blocks by Lionix BV. Both splitter designs were specified with 0.3 dB excess loss. Due to its wavelength independent splitting ratio, we chose to use y-splitters [20]. Our decision not to design our own splitter was driven by the risks of fabrication process deviations.

## 2.2 The OCT setup with the photonic integrated interferometer

Using 1x1 μm<sup>2</sup> waveguides, we designed and fabricated a Mach-Zehnder interferometer based photonic integrated circuit for OCT. An illustration of the circuit and the OCT system is given in Fig. 3(a). The circuit has three waveguides on the left edge and one waveguide on the right edge for coupling the light in and out. The waveguides on the entry-side (Fig. 3 left) were aligned with a fiber array that matched the pitch of the waveguides. The 1x1 μm<sup>2</sup> waveguides have a mode field diameter around 2.7 μm. To reduce the reflections at the waveguide ends, waveguides at both sides of the chip were angle polished at 8° to match the angle of the

commercially available angle polished fiber arrays, which is typically  $8^\circ$ . However, the effect of  $8^\circ$  angle polish is not optimal; from simulations we find that without angle polishing the return loss for  $TM_{00}$  is 14 dB, while the return loss with  $8^\circ$  polish angle is 20 dB. To achieve return loss level of 60 dB, which is typical for FC/APC connectors,  $24^\circ$  polish angle is needed.

The SLED (Previu/Thorlabs, Newton, USA) of the system has 1320 nm center wavelength, 100 nm full width half maximum (FWHM) bandwidth and 11.5 dBm power. The power of the SLED is reduced to 3.5 dBm to prevent saturation of the camera as the reference arm power in the current design cannot be adjusted and the power at the sample was  $-10$  dBm ( $100 \mu\text{W}$ ). All splitters in the circuit are symmetric  $y$ - splitters and have 50/50 splitting ratio. As depicted in Fig. 3(a), light from the SLED is coupled to the chip via the fiber array and split on the chip by splitter s1. The upper waveguide after splitter s1 guides light to splitter s2. From there the light exits the chip and is collimated by an achromatic lens ( $f = 2.97$  mm, NA = 0.6, C660TME-C, Thorlabs, gun2013ayNewton, USA). The collimated light is sent to an x-y scanner, which consists of a galvanometric x-y mirror pair (Thorlabs, Newton, USA) and a scan lens (LSM03, Thorlabs, Newton, USA).

Light reflected from the sample is collected via the same path and coupled back into the chip. Inside the chip, the light is split into two arms by splitter s2. Only the light in the lower arm is utilized and combined with the reference arm at combiner s4. The reference arm starts at the lower branch of splitter s1 and is comprised of a 190 mm long planar spiral. After passing the spiral, via splitter s3, half of the light signal is sent to a power monitor and the other half is combined with light from the sample arm at combiner s4. The power monitor is used to monitor the alignment stability of the fiber array while setting up the system. After combiner s4, the interference of the reference and sample arms is sent to the spectrometer. The all-reflective Czerny-Turner spectrometer contains a 1024 pixel InGaAs line camera with 47 KHz line rate (SU1024LDH-1.7RT, Sensors Unlimited Inc., Princeton, USA). The spectrometer has 0.125 nm spectral resolution, maximum imaging range of 3.4 mm in air and  $-17$  dB roll-off over the entire imaging range. The galvo scanner and the spectrometer camera are controlled with custom-built software implemented in LabVIEW (National Instruments, Austin, USA). An image of the part of the setup, which contains the integrated interferometer chip, is shown in Fig. 3(b). The standard die size in this fabrication run was  $16 \times 33 \text{ mm}^2$ , which is the size of the chip seen in Fig. 3(b). The size of the interferometer PIC design on this chip is  $10 \times 33 \text{ mm}^2$ .

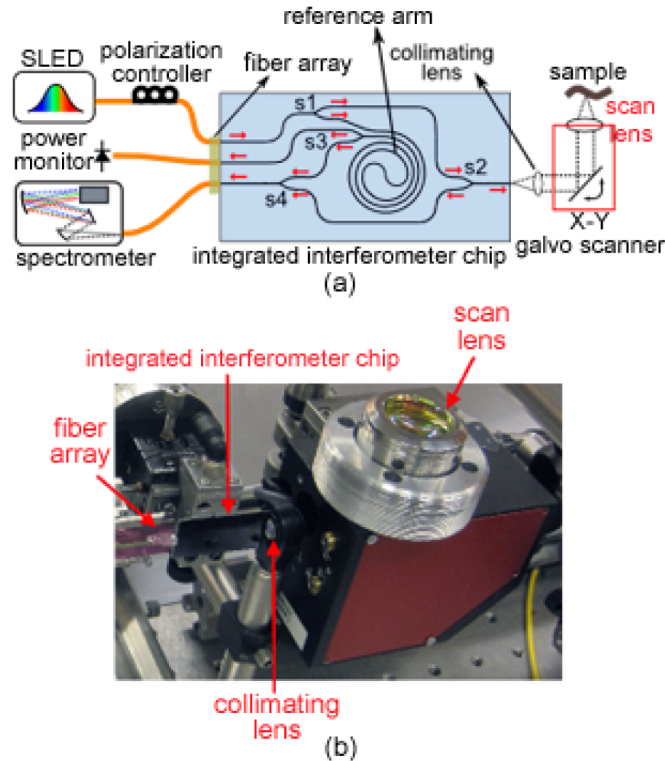


Fig. 3. (a) Schematic layout of the OCT setup with the integrated interferometer chip. (b) Photograph of the setup, where the fiber array, the integrated interferometer chip and the scan lens are seen.

### 3. Device characterization and *in vivo* human skin imaging

After aligning the setup, the polarization of light from the SLED was adjusted by monitoring the OCT signal from a mirror. If the polarization is not properly adjusted, while measuring reflectance from a mirror, there would be two peaks corresponding to the fundamental TE and TM modes, designating the two polarization states with different group indices. As the  $TM_{00}$  mode would cause lower dispersion than  $TE_{00}$  mode, we chose the TM peak and maximized it by adjusting the polarization controller. Without dispersion compensation, the TM peak was sharper than the TE peak.

#### 3.1 Axial resolution and sensitivity

To characterize the system's axial resolution and sensitivity, reflection from a mirror positioned at 0.25 mm far from the zero delay line was measured. The data processing consisted of background subtraction, rescaling, spectral shaping (apodization) and dispersion compensation. For spectral shaping, the spectrum was corrected for the envelope and multiplied with a fitted 90 nm FWHM Gaussian window, which would yield 10  $\mu\text{m}$  theoretical resolution in air. The dispersion mismatch between the two arms of the system was compensated in software by a dispersion search algorithm based on a previous implementation [21] but enhanced to search and compensate for more than 3rd order dispersion. Together with the large difference of material dispersion in the two arms, the waveguide dispersion causes a strong non-linear shift in the spectral phase that can be modeled as a high order Taylor series. To overcome strong noise and high error with high order optimization, the optimization algorithm was split into two independent steps. For a first approximation, signal from a mirror was used to find an initial set of dispersion parameters.

The search was guided using dispersion parameters obtained from simulated TM<sub>00</sub> effective index values with respect to wavelength. In a further step, the obtained spectral phase was set as the starting point for dispersion optimization on the biological signal utilizing the image entropy as a sharpness measure. The final dispersion parameter values were found within a factor of 3 to the parameters found from simulations. The discrepancy can be attributed to numerical errors in simulations, differences between the simulated and fabricated waveguides and noise in the data. The measured axial resolution of the system was 14  $\mu\text{m}$  with conventional 3rd order dispersion correction and reached the theoretical limit after correction of the orders up to 10th order.

For sensitivity estimation, first we measured the sensitivity of an OCT system with fiber based splitters and a free space reference arm. The spectrometer, the scanner and the software were the same. The spectrometer camera was operated at 47K A-scans/s. This setup was an OCT for dermatological imaging operating with 2.5 mW power on the sample. The sensitivity of the system was calculated by the ratio of the peak to the standard deviation of the noise floor around the peak. The measured sensitivity of this system with 2.5 mW on the sample was 94 dB, while the shot noise limited, lossless system would have 111 dB sensitivity. The setup had total of 7 dB loss in the sample arm, due the losses at the scanner and the spectrometer. Thus, the system performance was degraded by 10 dB due to other noises sources such as intensity and readout noise. Then we measured the sensitivity of that fiber system at 100  $\mu\text{W}$ , which was the maximum power level on the sample achievable with the chip. The measured sensitivity was 73 dB, while shot noise limited sensitivity at that power level would be 97 dB. Taking the 7 dB spectrometer and scanner losses into account, we may conclude that other noise sources degraded the sensitivity by 17 dB. The sensitivity of the system with the integrated interferometer chip was measured with 100  $\mu\text{W}$  on the sample. The sensitivity was 65 dB, which is 8 dB less than the sensitivity of the fiber system using the same power level on the sample. Considering the 3 dB loss at splitter s2 and the 4.5 dB loss at the chip to fiber array interface the total loss in the sample arm was 7.5 dB. Here, for simplicity, we ignored the excess losses of the y-splitters ( $2 \times 0.3$  dB) and the propagation loss in the sample arm (0.7 dB) as the fiber splitter used in the fiber setup had around 1 dB excess loss. Thus, except the 7.5 dB extra loss in the sample arm, the sensitivity obtainable with the chip is comparable with the setup with fiber components.

**Table 1. Sensitivity and loss data.**

System	P <sub>sample</sub> ( $\mu\text{W}$ )	Sensitivity shot noise limited (dB)	Sensitivity measured (dB)	spectrometer + scanner loss (dB)	chip losses (dB)	sensitivity degradation from other noise sources (dB)
fiber-based	2500	111	94	7	-	10
fiber-based	100	97	73	7	-	17
with integrated interferometer	100	97	65	7	7.5	17.5

### 3.2 *In vivo* human finger skin imaging

To evaluate the system, we imaged a human fingertip and finger mid-joint *in vivo*. The fingertip image shown below in Fig. 4 is a median projection of 100 OCT B-scans to reduce speckle and increase sensitivity by  $\sim 10$  dB. In B-scan images the axial direction is scaled by 1.33 to account for the refractive index of tissue. Different layers of fingertip such as the stratum corneum (SC), viable epidermis (VE), papillary dermis (PD) and reticular dermis (RD) can be differentiated in the image. The viable epidermis appears as a waved and brightly scattering layer because of the dermal papillae. The dermal-epidermal junction is not well demarcated due to its undulating nature (marked by the yellow curve). The papillary dermis can be identified by the presence of dermal papillae. It is separated from the flat reticular

dermis by the less scattering region of rete subpapillare. The dermis appeared as a bright scattering layer. Sweat ducts traversing to the epidermal surface are visible.

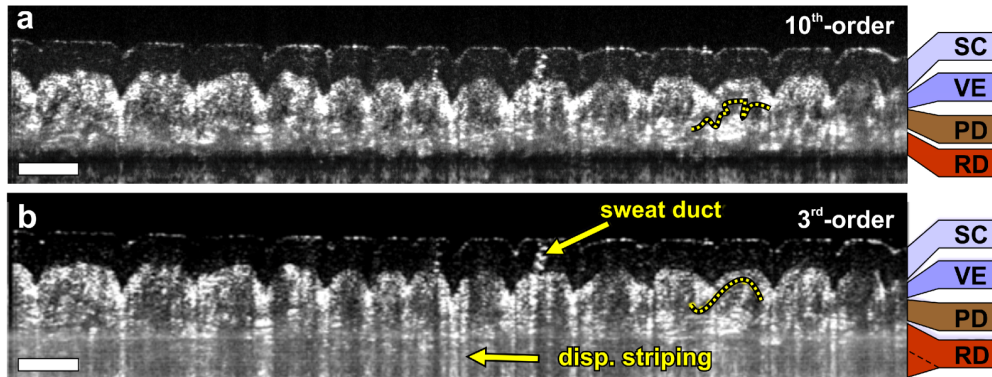


Fig. 4. OCT cross section (sum projection of 100 B-scans) of a fingertip. SC: stratum corneum, VE: viable epidermis, PD: papillary dermis, RD: reticular dermis. The yellow dotted curve marks the dermal-epidermal junction. The scale bars represent 500  $\mu\text{m}$  length. a) after 10th order and b) after 3rd order dispersion compensation. Latter depicts dispersive striping.

The comparison of the two sub Figs. 4(a) and 4(b) shows that higher order dispersion correction is crucial in this system configuration with a highly dispersive reference arm. In the case where even very small values of the higher order coefficients are accounted for (Fig. 4(a)), the tomogram appears more crisp and allows to follow the fine structure more precisely. It displays an improved sensitivity that is well evident as an improved visibility of the stratum corneum, and suppressed vertical dispersive striping that typically overcasts the end of the reticular dermis (see dashed portion of RD-marker in Fig. 4(b)). The dark region following the reticular dermis is due to signal attenuation with depth as the signals at that depth are below the threshold level. Ideally, below that region we should not see any signal. However, the zero delay line was chosen to be inside the tissue and due to remaining DC and autocorrelation signals, which are dispersed, a bright band appears below the dark region.

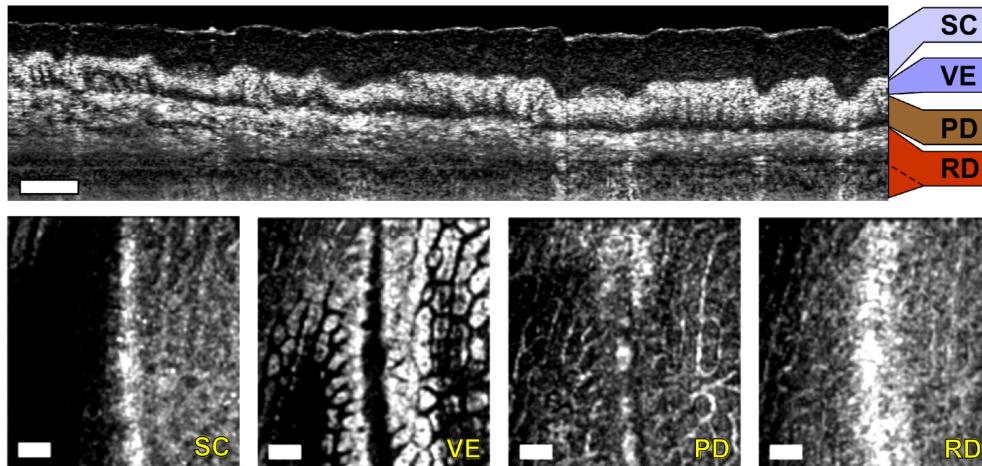


Fig. 5. OCT cross-section (sum projection of 28 B-scans) and en-face views of a finger midjoint. The yellow curve marks the dermal-epidermal junction. SC: stratum corneum, VE: viable epidermis, PD: papillary dermis, RD: reticular dermis. The scale bars of the cross-sectional image represent 500  $\mu\text{m}$  length, while the scale bars of the en-face images represent 1 mm length

Cross-sectional and *en-face* views of OCT images obtained from the finger mid-joint are shown in Fig. 5. In the cross sectional image, different epidermal and dermal sub-layers of thick skin are visible. The morphological variations of different skin layers can be seen in the *en-face* images. The characteristic nature of different layers such as the light-scattering nature of the stratum corneum layer, the epidermal rete ridges in the viable epidermis, dermal papilla in the papillary dermis and the fiber-rich reticular dermis is seen in these OCT images.

#### 4. Discussion

The characterization of the system and *in vivo* finger images suggest that  $\text{Si}_3\text{N}_4/\text{SiO}_2$  based box shaped waveguide technology is a viable platform for passive PICs for OCT. As demonstrated in this study, all splitters and the reference arm can be realized on a single substrate within a small area with high volume manufacturing technology. Furthermore, a single wafer can accommodate tens of such interferometers for parallel OCT and implementation on single substrate will increase the stability of the interferometers. To further increase the appeal of this platform for OCT, there are several opportunities related to coupling efficiency, dispersion, reference arm power adjustment and integration with active components.

The 65 dB sensitivity of the system could be improved in several ways. As shown in Table 1, there is a 17 dB additional degradation of the sensitivity, likely to be due to intensity and readout noise. By changing the reference arm power and camera settings 10 dB higher sensitivity might be obtainable. In an integrated interferometer, the reference arm power can be adjusted by incorporating of an integrated broadband variable optical attenuator. Integrated optical attenuators usually consist of a small Mach-Zehnder interferometer with specially designed couplers and phase tuning mechanism [22]. Further reduction in noise can also be achieved by designing the PIC for swept source OCT with balanced detection. Using a Michelson configuration will eliminate the extra splitter (splitter s2) and provide additional 3 dB increase in sensitivity. Obviously, reducing the 4.5 dB fiber to chip coupling loss will also have a significant effect on the sensitivity.

Coupling the light beam efficiently from standard single mode fibers to PICs is challenging, as the mode field diameter of integrated waveguides are smaller than the mode field diameter of the standard single mode fiber. We used a standard single mode SMF28 fiber array that had 4.5 dB loss per coupling to the chip. However, there are options that can provide  $< 0.5$  dB loss per coupling. One common solution used to couple light into integrated waveguides is to use lensed fibers where the tip of a standard fiber is shaped to provide a reduced beam waist that can match the mode size of the waveguides. A similar solution is to use high numerical aperture fibers such as UHNA fiber series from Nufern (East Granby, USA). Such fibers can provide mode sizes of few microns and can be spliced to single mode fibers with 0.12 dB splicing loss [23]. Another solution to increase the coupling efficiency is to implement spot size converters, which can adiabatically transform the small waveguide mode profile to a larger one [24].

Dispersion compensation is a challenge in an integrated interferometer which consists of dispersive waveguides and has large arm length mismatch. In addition to software compensation, waveguide dispersion minimization should be considered. If design flexibility is provided, dispersion of the waveguides can be further minimized by changing the geometry of the waveguides (e.g. width, height,  $\text{Si}_3\text{N}_4$  layer thickness). For example, simulations of GVD with varying  $\text{Si}_3\text{N}_4$  layer thicknesses show that changing the  $\text{Si}_3\text{N}_4$  layer thicknesses from 50 nm to 45 nm, brings the GVD of  $\text{TM}_{00}$  from  $-205$  ps/km.nm to  $-75$  ps/km.nm. Further reducing the  $\text{Si}_3\text{N}_4$  layer thickness to 40 nm cause a sign change in the GVD and it becomes 22 ps/km.nm. If  $\text{Si}_3\text{N}_4$  layer thickness can be reproducibly controlled within few nanometers, the GVD can be significantly reduced.

To achieve high resolution in OCT, in addition to a broadband source, splitters need to be sufficiently broadband. Y-splitters are broadband, however, they are known to have higher

excess loss than directional couplers. The excess loss of y-splitters is mainly due to the fabrication limited blunt at the junction, which also causes some back reflection. Although directional couplers have smaller bandwidths compared to y-splitters and more prone to fabrication tolerances, they usually have lower insertion losses than y-splitters and do not have back reflection. Ideally, directional couplers are lossless. Their insertion losses can result due to fabrication related phenomena such as incomplete gap opening during etching or presence of more sidewall roughness inside the gap than outside the gap. An attractive splitter design for OCT is the adiabatic coupler, which is a modified directional coupler consisting of waveguides of varying widths rather than conventional uniform waveguides. Although such couplers are several times longer than general directional couplers, they can be designed to have > 200 nm bandwidth [17].

The box shaped waveguides utilized in this work are birefringent and provide the advantages of polarization maintenance such as improved polarization stability of the interferometer and elimination of the polarization controllers in the sample and reference arms. In a birefringent interferometer, light should be coupled to only one of the polarization states. Otherwise, for a single reflector two peaks at different locations would appear, corresponding to each polarization state. In our setup, we optimized the polarization using a paddle-based fiber polarization controller to couple the light to the mode with lower GVD.

In general, interferometers in OCT systems are Michelson type. The type of interferometer does not significantly affect the SNR, as long as it is made from ideal waveguides and is power conserving [25]. However, integrated waveguides are not ideal and have significantly higher loss compared to fibers due to sidewall roughness imposed by current manufacturing techniques. As the resolution of lithographic processes improves, the sidewall roughness reduces. The optical loss within waveguides fabricated in this study is <0.14 dB/cm while typical fiber loss is <0.35 dB/km. The roughness on the sidewall of a waveguide scatters the light in all directions and is mostly radiated away, but some of it will scatter backward in the waveguide. In Michelson configuration, backscattering due to the sidewall roughness in the sample and reference arm waveguides can degrade the system performance in high refractive index contrast waveguides, as we demonstrated previously in silicon [15]. In the multi project wafer run used for this manufacturing step, we had limited mask space, which was sufficient only for one interferometer and we chose to design a Mach-Zehnder type interferometer, in case sidewall roughness effects are significant. Ideally, different types of interferometers can be fabricated on the same chip and their performances can be compared.

In principle, the waveguide technology employed in this paper can be used to design an integrated spectrometer similar to the one demonstrated by Akca et. al [17]. Combining such a spectrometer with an integrated interferometer with an on-chip reference arm will be an important step towards OCT-on-a-chip. For a complete integrated OCT system, hybrid integration [26] of an SLED and a photodetector array with this waveguide technology can be investigated.

## 5. Conclusion

We have demonstrated an OCT system that uses a PIC consisting of splitters and a reference arm. The system shows a potential of the  $\text{Si}_3\text{N}_4/\text{SiO}_2$  TriPleX<sup>TM</sup> platform for further integration of other OCT components and parallelization. Although we were able to obtain *in vivo* images from a human finger, the sensitivity is 8 dB less than a fiber-based system. Thus, in order to proceed with more complex PICs for OCT using this material system, further optimization is necessary. Further integration approaches of active devices such as light sources and detectors will open a road towards fully integrated OCT systems.

## Acknowledgments

This work was supported by the Smartmix MEMPHIS project the Netherlands Ministry of Economic Affairs and the Netherlands Ministry of Education, Culture and Science and Gent

University–Methusalem project “Smart Photonic Chips”, Medical University Vienna, European Union project FUN OCT (FP7 HEALTH, contract no. 201880), Bern University of Applied Sciences, Swiss National Science Foundation project 320030\_146021, and FWF-NFN ‘Photoacoustic imaging in biology and Medicine’. We would like to thank Arne Leinse and Marcel Hoekman from Lionix BV for useful discussions related to the photonics integrated circuit fabrication and Sesilia Kriswandhi from Phoenix BV for help with mask design.